The Effect of Single versus Polycrystalline Cathode Particles on All-Solid-State Battery Performance

Seyedhosein Payandeh, Christian Njel, Andrey Mazilkin, Jun Hao Teo, Yuan Ma, Ruizhuo Zhang, Aleksandr Kondrakov, Matteo Bianchini, and Torsten Brezesinski**

Lithium-thiophosphate-based all-solid-state batteries (ASSBs) are increasingly attracting attention for high-density electrochemical energy storage. In this work, the cycling performance of single and polycrystalline forms of $LiNi_xCo_yMn_zO_2$ (NCM, with ≥83% Ni content) cathode active materials in ASSB cells with an $Li_4Ti_5O_{12}$ composite anode is explored, and the advantages and disadvantages of both morphologies are discussed. The virtual lack of grain boundaries in the quasi-single-crystalline material is found to contribute to improved stability by eliminating the tendency of Ni-rich NCM particles to crack during cycling, due to volume differences between the lithiated and delithiated phases. Although the higher crack resistance mitigates effects of chemical oxidation of the lithium thiophosphate solid electrolyte, the cells suffer from electrochemical side reactions occurring at the cathode interfaces. However, coating the single-crystal particles with a protective $LiNbO_3$ overlayer helps to stabilize the interface between cathode active material and solid electrolyte, leading to a capacity retention of 93% after 200 cycles (with $q_{dis} \approx 160$ mAh g_{NCM}^{-1} or 1.7 mAh cm^{-2} at C/5 rate and 45 °C). Overall, this work highlights the importance of addressing electro-chemo-mechanical phenomena in ASSB electrodes.

1. Introduction

In all-solid-state batteries (ASSBs), the flammable organic liquid electrolyte is replaced by a superionic solid electrolyte (SE), offering a safer alternative to conventional Li-ion batteries (LIBs). SEs prevent detrimental chemical crosstalk between the electrodes and their higher Li^+ transference number ($t_{Li+} \approx 1$ for inorganic SEs, compared to 0.2–0.5 for aprotic electrolytes)

allows increased (dis)charge rates.[1–3] Apart from that, improvements in energy density can be achieved by using high-voltage/capacity cathodes and Li metal anodes or by bipolar stacking.[4,5] However, ASSBs typically experience faster capacity loss because of the narrow stability window of most SEs and electro-chemo-mechanical degradation.[6–8]

Different kinds of SEs may be used in ASSBs, with each type having its own challenges.[9] Polymer-based electrolytes show limited electrochemical stability and are incompatible with high-voltage cathodes.[10–12] Oxides are brittle, making them susceptible to cracking upon volume variation of the storage material(s) during cycling.[13,14] Hydroborates are difficult to synthesize and are primarily compatible with Na-ion battery systems.[15–18] Halide electrolytes offer a high electrochemical oxidative stability and can therefore be paired with high-voltage cathodes,[19] but they suffer from limited cathodic stability causing decomposition reactions at low potentials,[20] and usually contain costly elements.[21] Sulfides have a narrow electrochemical stability window.[22] However, they exhibit favorable mechanical properties and show excellent performance in combination with coated (e.g., by $LiNbO_3$) cathode active materials (CAMs).[22–25] Thus, a lithium thiophosphate SE, argyrodite Li_6PS_5Cl, was employed in this study.

S. Payandeh, A. Mazilkin, J. H. Teo, Y. Ma, R. Zhang, A. Kondrakov,
M. Bianchini, T. Brezesinski
Battery and Electrochemistry Laboratory (BELLA)
Institute of Nanotechnology
Karlsruhe Institute of Technology (KIT)
Hermann-von-Helmholtz-Platz 1, 76344 Eggenstein-Leopoldshafen,
Germany
E-mail: a.payande88@gmail.com; torsten.brezesinski@kit.edu

The ORCID identification number(s) for the author(s) of this article can be found under https://doi.org/10.1002/admi.202201806.

C. Njel
Institute for Applied Materials—Energy Storage Systems (IAM-ESS)
Karlsruhe Institute of Technology (KIT)
Hermann-von-Helmholtz-Platz 1, 76344 Eggenstein-Leopoldshafen,
Germany
C. Njel
Karlsruhe Nano Micro Facility (KNMFi)
Karlsruhe Institute of Technology (KIT)
Hermann-von-Helmholtz-Platz 1, 76344 Eggenstein-Leopoldshafen,
Germany
A. Mazilkin
Institute of Nanotechnology
Karlsruhe Institute of Technology (KIT)
Hermann-von-Helmholtz-Platz 1, 76344 Eggenstein-Leopoldshafen,
Germany
A. Kondrakov, M. Bianchini
BASF SE
Carl-Bosch-Str. 38, 67056 Ludwigshafen, Germany

**ADVANCED
SCIENCE NEWS**
www.advancedsciencenews.com

**ADVANCED
MATERIALS
INTERFACES**
www.advmatinterfaces.de

In recent years, many efforts have been made to increase the ionic conductivity of SEs and to understand the fundamental principles of cathode coatings, while little attention has been paid to the CAM morphology and its effect on battery performance.[26–29] The cathode is considered the most critical component of the battery in determining its energy density and cost. Up to now, most of the reported ASSBs are based on polycrystalline (PC) forms,[30] where the particles already degrade to some degree during the high stack-pressure cell assembly.[31,32] In addition, the anisotropic volume changes of the randomly oriented primary grains in PC cathodes lead to cracking and disintegration of the secondary particles.[33] This issue is exacerbated by increasing the Ni content in the state-of-the-art CAM, $LiNi_xCo_yMn_zO_2$ (NCM or NMC), because of the higher achievable state of charge (and larger absolute volume variation) for a given cutoff voltage.[34–37] In this regard, crack-resistant, single-crystalline (SC) NCM materials have been implemented recently in LIBs and ASSBs. The absence of grain boundaries in such CAMs eliminates their tendency for intergranular fracture, thereby contributing to improved capacity retention by preventing exposure of reactive surfaces to the electrolyte (i.e., formation of resistive interfaces and interphases) and contact loss.[31,32,38–41]

In the present work, we compare the performance of SC and PC Ni-rich (≥83%) NCM cathodes in lithium-thiophosphate-based ASSB cells. For a proper comparison, CAMs of similar size and bulk/surface composition were selected and studied by scanning electron microscopy (SEM), focused-ion beam (FIB) scanning transmission electron microscopy (STEM) in dark-field mode, energy-dispersive X-ray spectroscopy (EDS), electron energy-loss spectroscopy (EELS), X-ray diffraction (XRD), X-ray photoelectron spectroscopy (XPS), differential electrochemical mass spectrometry (DEMS) and pressure measurements. Particle fracture and formation of oxygenated sulfur and phosphorus side products at the SE|CAM interface were found to lead to accelerated degradation of the PC cathode. The performance of the SC cathode was further improved by surface modification of the CAM, achieving ≈80% capacity retention after 400 cycles (≈93% after 200 cycles).

2. Results and Discussion

2.1. Characterization of the SC and PC Cathode Materials

PC $LiNi_{0.85}Co_{0.10}Mn_{0.05}O_2$ (NCM851005, referred to as PC-85) and SC $LiNi_{0.83}Co_{0.12}Mn_{0.05}O_2$ (NCM831205, referred to as SC-83) were chosen as CAMs in this study. PC-85 with a slightly higher Ni content (85%) than SC-83 (83%) was employed, since it has been specially synthesized for ASSB applications. Both materials had a similar D50 particle size, with ≈5 µm for PC-85 and ≈4 µm for SC-83.

XPS measurements were conducted on the pristine samples to examine their surface composition. **Figure 1**a presents the O 1s spectrum collected from the SC and PC CAMs. The signals observed at binding energies of 532.8 eV (orange) and 528.8 eV (red) can be attributed to oxygen from carbonate/C—O-type species and NCM, respectively.[41] Additionally, a peak around 530.3 eV (green) was detected, indicating the presence of NiOOH (i.e., oxygen from metal hydroxide species).[42] The intensity of this peak was higher for SC-83, presumably because of a post-treatment (washing) step that was applied after synthesis to reduce the residual lithium content (surface Li_2CO_3 and/or LiOH). Note that Li^+/H^+ exchange takes place to some degree during washing.[43] Similar impurities have been observed by Fantin et al.[41] The difference in peak area/intensity for the NCM oxygen signal between the SC and PC CAMs can be explained by the presence of NiOOH and differences in the amount of carbon-based surface species.

The SEM images of the PC and SC CAMs in Figure 1b show that PC-85 exhibited a secondary particle morphology. In contrast, SC-83 consisted of partially agglomerated primary particles (monolithic grains), demonstrating that the sintering only resulted in a semi-SC nature. Cross-sectional STEM corroborated the microscopy results (Figure 1c), and EDS mapping revealed the presence of carbon-containing species on the top surface of the CAM particles, which agrees with the XPS data. Similar Li_2CO_3 contents of 0.15 and 0.20 wt% were found by acid titration for PC-85 and SC-83, respectively. The same holds for the specific surface area ($S_{BET} ≈ 0.6–0.7$ m² g⁻¹). Furthermore, powder XRD characterization revealed the expected
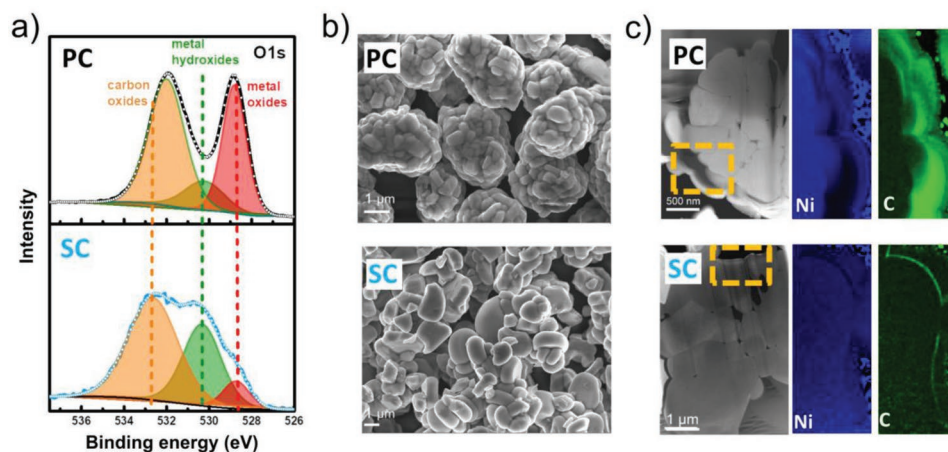

Figure 1. a) X-ray photoelectron spectra of the O 1s core-level region of PC-85 (black) and SC-83 (blue). b) Low-magnification SEM images. c) Cross-sectional STEM images and corresponding Ni and C maps from EDS.
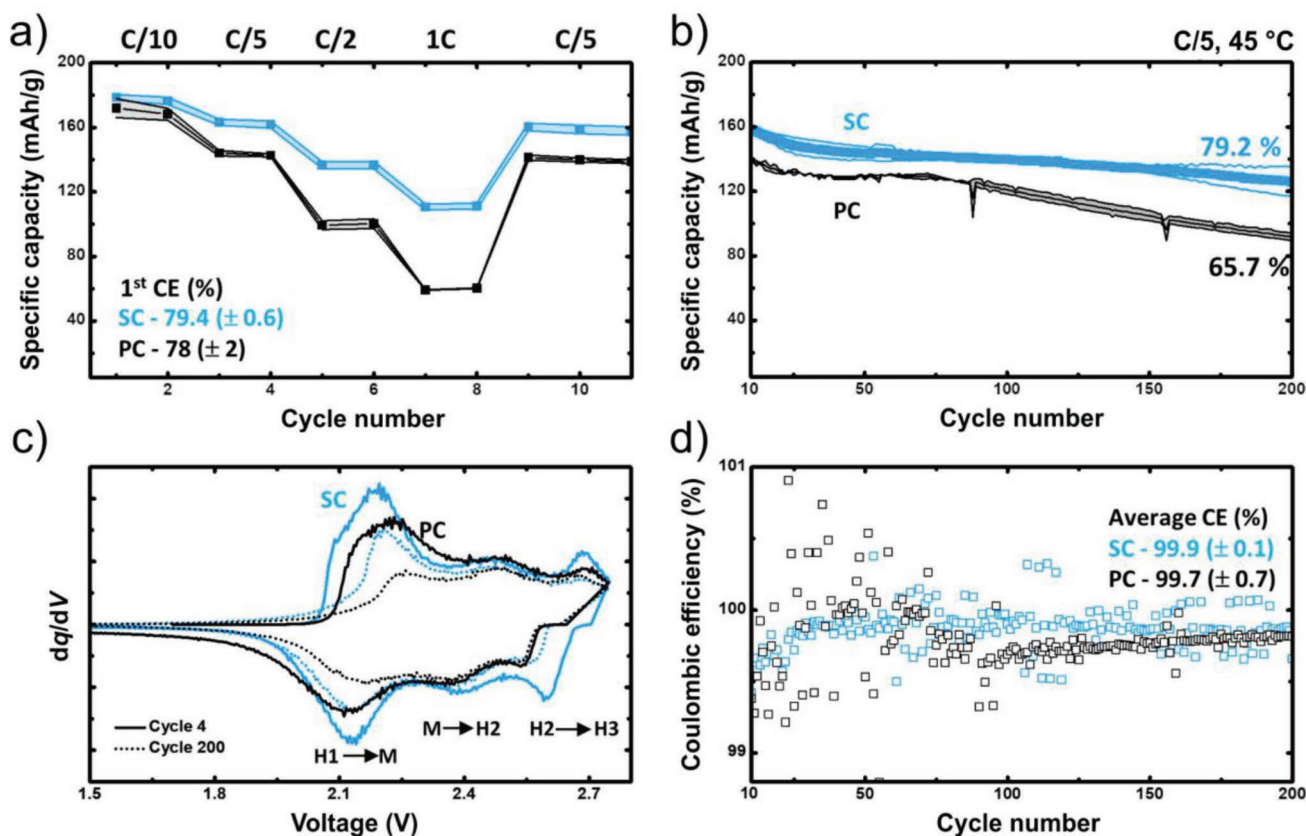
Figure 2. a) Rate performance of the ASSB cells with PC-85 (black) or SC-83 (blue). b) Long-term cycling performance at C/5 after initial rate capability testing. c) Differential capacity plots for the 4th and 200th cycles. d) Coulomb efficiencies. The cells were cycled at 45 °C between 1.35 and 2.75 V versus $Li_4Ti_5O_{12}/Li_7Ti_5O_{12}$. The data are the average of two independent cells.

layered structure of NCM materials with space group $R–3m$. A Ni^{2+}/Li^+ cation mixing (substitutional defects) of 1.3% for PC-85 and 2.7% for SC-83 was determined from Rietveld analysis (Figure S1, Supporting Information). The characterization results are summarized in Table S1 (Supporting Information). Overall, we believe that the similarities allow for a fair comparison between the two cathode morphologies in ASSBs.

2.2. Cycling Performance of the SC and PC Cathode Materials

To evaluate the cycling performance and stability of the PC-85 and SC-83 CAMs in pellet-stack cells ($\approx$11 mg_{NCM} cm^{-2} areal loading), argyrodite Li_6PS_5Cl with an ionic conductivity of $\sigma_{ion,rt} \approx 2$ mS cm^{-1} and $Li_4Ti_5O_{12}$ (LTO) were used as SE and anode material, respectively. The LTO anode has been shown to be reasonably stable against Li_6PS_5Cl, and its zero-strain behavior (negligible volume changes during Li insertion/extraction) allows mechanical degradation to be attributed exclusively to the cathode side.[44] **Figure 2** shows the cycling and rate performance data for the uncoated cathodes at 45 °C. The cells delivered similar first-cycle specific charge capacities (see voltage profiles at C/10 rate in Figure S2, Supporting Information). However, the higher initial Coulomb efficiency (CE) of (79.4 ± 0.6)% for SC-83, compared to (78 ± 2)% for PC-85, resulted in a larger

specific discharge capacity of $q_{dis} = (179 \pm 2)$ mAh g_{NCM}^{-1} versus (172 ± 6) mAh g_{NCM}^{-1}. The difference in cyclability became even more pronounced upon increasing the C-rate (Figure 2a), suggesting improved contact between the SE and CAM particles in the SC-83 cathode. The same behavior has been observed previously and attributed to the decreased number of grain boundaries.[45] SC cathodes provide continuous conduction paths through the single grains, which may positively affect the rate performance (depending on the particle size).

The stability of the cells over 200 cycles at C/5 after rate capability testing and the corresponding CEs are shown in Figures 2b,d. The SC-83 cells delivered larger capacities and showed an improved capacity retention of $\approx$79% (from the 10th cycle onward), compared to $\approx$66% for PC-85. The CE of the SC-83 cells increased initially and then stabilized at $(99.9 \pm 0.1)\%$, while that of the PC-85 cells underwent a sudden decrease after about 70 cycles, eventually leading to accelerated capacity decay. This could be a sign of mechanical degradation (particle fracture, void formation, contact loss, etc.), thereby helping to explain the lower average value of the CE $[(99.7 \pm 0.7)\%]$.[8,46]

The differential capacity curves in Figure 2c show the characteristic redox peaks previously observed for Ni-rich NCM CAMs in LIBs.[47] They are related to the phase transitions from H1 (hexagonal) to M (monoclinic), M to H2 and H2 to

ADVANCED
SCIENCE NEWS
www.advancedsciencenews.com

ADVANCED
MATERIALS
INTERFACES
www.advmatinterfaces.de

H3 as lithium is extracted from the cathode. The loss of available lithium is evident from the fading of these peaks. Aging strongly affected the H1 to M transition at relatively low cell voltages of ≈2.2 V versus $Li_4Ti_5O_{12}/Li_7Ti_5O_{12}$ (≈3.75 V vs Li^+/Li). At this stage, the cathode is in a highly lithiated state and has a relatively low apparent lithium-diffusion coefficient.[33,48] This means that the formation of resistive interfaces/interphases and contact loss between CAM and SE directly affect the (de)lithiation behavior of the cathode and the subsequent capacity decay. Thus, the lower peak intensity observed for PC-85 after cycling hints toward a higher degree of adverse side reactions and/or contact loss. Apart from that, the data further indicate that the H2 to H3 transition in SC-83 was also affected during extended battery cycling.

2.3. Impedance Analysis, Volume Variation, and Cracking Behavior of the SC and PC Cathode Materials

To gain more insight into the reasons for the capacity fading, the cycled cells were probed using electrochemical impedance spectroscopy (EIS) and electron microscopy. Results from the EIS measurements are presented in **Figure 3**a.

Despite the increased cycling stability of the SC-83 cathode, a higher impedance was found for the cells using this CAM. This finding seems to be indicative of more degradation in general. We note that hydroxide impurities have been shown to increase the cell resistance by promoting decomposition of the SE.[41] In addition, a considerable difference was observed in the low-frequency Warburg components. The PC-85 cells showed a Warburg tail with a much steeper slope. Some recent studies suggested that the Warburg coefficient (D_w) can be used as an indication of contact loss due to particle fracture, among others.[8,49] The D_w can be determined from Equation S1 (Supporting Information) by plotting the real part of the impedance (Z_{RE}) versus the reciprocal root square of the frequency ($\omega^{-1/2}$). It is inversely proportional to the contact area (Equation S2, Supporting Information), assuming that the decomposition interphase at the SE|CAM interface is uniform. Figure 3b shows that the D_w of the PC-85 cells is larger by a factor of three compared with the SC-83 cells, suggesting a lower contact area between the cathode components after 200 cycles.

To visualize the electro-chemo-mechanical evolution of the samples, cross-sectional STEM was performed on the cathodes prior to and after cycling (Figure 3c). The images collected
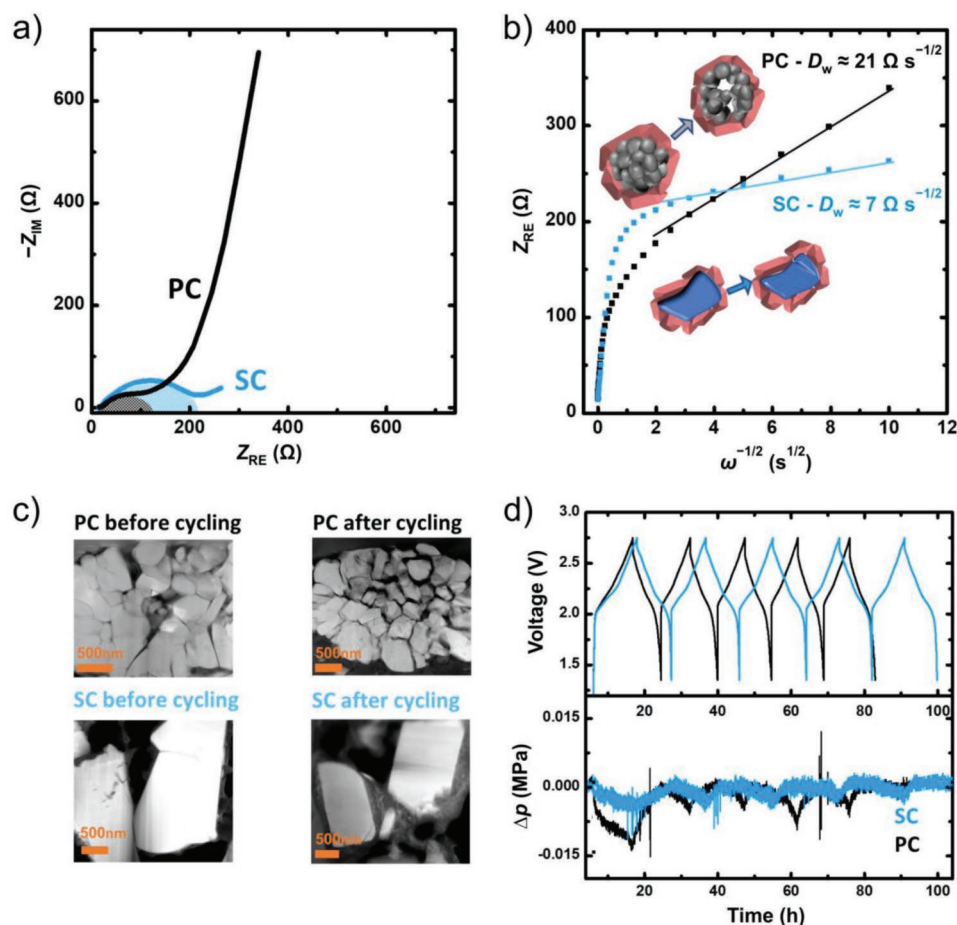

Figure 3. a) EIS plots of the ASSB cells with PC-85 (black) or SC-83 (blue) after cycling. b) The real part of the impedance versus the reciprocal root square of the frequency and corresponding linear fits to the data at low frequencies (<1 Hz). c) Cross-sectional STEM images of the cathode particles prior to and after cycling. d) In situ pressure analysis of cells cycled at C/10 rate and 45 °C between 1.35 and 2.75 V versus $Li_4Ti_5O_{12}/Li_7Ti_5O_{12}$.

from the pristine PC-85 secondary particles revealed partial intergranular cracking. This is due in part to the high pressure applied during the assembly of the pelletized cells, as mentioned above. Much less fracture was observed for the SC-83 CAM, indicating improved crack resistance (robustness). After cycling, PC-85 showed severe particle fracture, resulting in contact loss and cell degradation. However, no noticeable cracking occurred in the SC-83 material. This result is in line with observations from previous reports on SC cathodes.[31,40] Intragranular cracking was not evident from the imaging data.

Next, pressure monitoring of the cells was performed in situ to study the volume variation during cycling (Figure 3d).[8,50,51] The baseline of the force response was corrected and the signal converted into pressure change (Δp, uniaxial stress). The LTO anode experienced virtually no volume changes.[52] Thus, the signal is dominated by the expansion/contraction of the CAM particles. The volume contraction during delithiation (charge) caused a negative net pressure change, which was reversed upon subsequent discharge.[37] Larger absolute changes were observed for the PC-85 cells. In the first charge cycle, there was a factor of about two difference in Δp. It is noteworthy to mention that PC-85 delivered a lower specific capacity (205 mAh g_{NCM}^{-1}) than SC-83 (226 mAh g_{NCM}^{-1}), corresponding to a lower degree of delithiation. We attribute the larger changes in Δp to the secondary particle morphology and the anisotropic volume variation in the randomly oriented primary grains. This also provides an explanation for the differences in particle cracking and cyclability seen in Figure 3c and Figure 2b, respectively. However, particle fracture can also be related, at least to some degree, to the (electro)chemical side reactions occurring at the SE|CAM interface, as shown recently by Han et al.[40]

2.4. Cathode Interface Degradation and Gas Analysis

As discussed in the previous section, the higher impedance of the SC-83 cells is somewhat contradictory to their superior cycling performance. XPS measurements were thus conducted on the cathodes prior to and after cycling to identify the SE decomposition products formed at the interfaces. The S 2p detail spectra in **Figure 4**a were fitted with peak doublets separated by 1.2 eV and with a 2:1 area ratio. The main doublet with the S $2p_{3/2}$ peak located at a binding energy of 161.6 eV (in green) corresponds to the PS_4^{3-} tetrahedra in the argyrodite SE structure.[44,53] That at ≈163.0 eV (in wine) and the minor signal at ≈167.0 eV (in orange) can be assigned to bridging sulfur atoms from polysulfides (denoted as P-S-P) and sulfite species, respectively.[54] The doublet with the S $2p_{3/2}$ peak around 160.4 eV (in yellow) is due to Li_2S impurities remaining from the synthesis and/or free S^{2-} ions.[55] The S 2p data collected from the composite cathodes prior to cycling were similar to those of the pristine Li_6PS_5Cl SE, with only a slight shift observed for the oxidized sulfur (polysulfide) species. Chemical reactions between the CAM and SE particles occurring during electrode preparation and cell assembly can therefore be largely ruled out (see also Figure 4c). The S 2p spectra recorded after 200 cycles are shown in Figure 4b. For both samples, the intensity of the main doublet decreased and that of the polysulfide
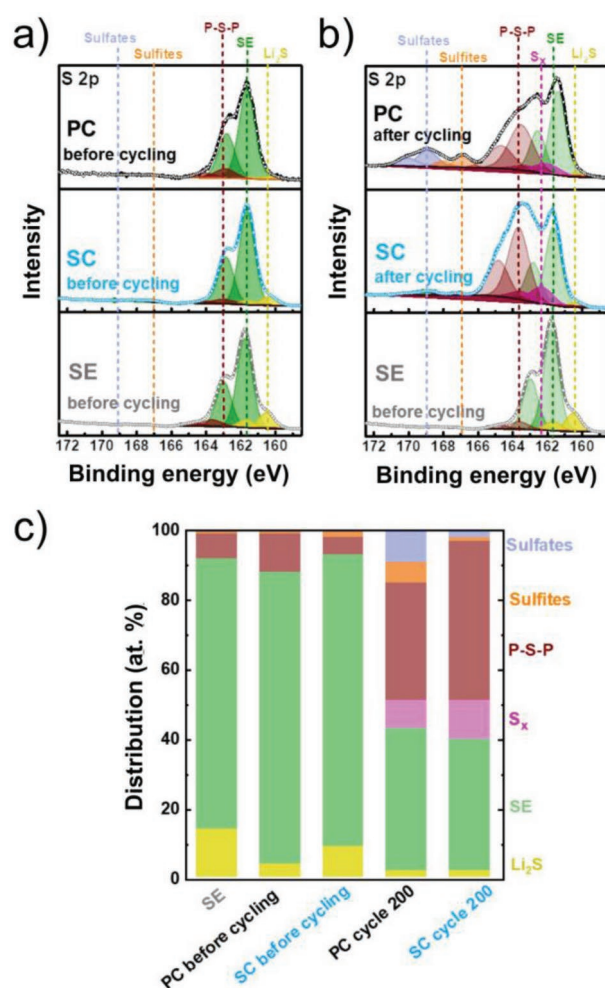

Figure 4. X-ray photoelectron spectra of the S 2p core-level region of pristine SE (gray) and composite cathodes with PC-85 (black) or SC-83 (blue) a) prior to and b) after cycling. c) Summary of the surface compositions.

peaks increased strongly, indicating SE degradation. Furthermore, new doublet peaks appeared at binding energies of 162.3 eV (in pink) and 169.0 eV (in bright purple), which can be attributed to terminal sulfur atoms (denoted as S_x) and sulfate, respectively.

A summary of the surface compositions from XPS is given in Figure 4c. Severe SE degradation took place upon cycling, as expected for uncoated CAMs in thiophosphate-based cells. While a higher atomic percentage of oxidized sulfur species was found for the SC-83 cathode, the PC-85 cathode showed the formation of more oxygenated side products. The corresponding P 2p detail spectra of the pristine SE and the composite cathodes are shown in Figure S3 (Supporting Information) and confirm this trend. The different degradation behavior of the SE, which is presumably also responsible for the higher cathode interfacial resistance in the case of SC-83, seems to be related to the NiOOH-like phases present on the CAM particle surface. However, the improved cycling performance of SC-83 over PC-85 demonstrates that the resistance buildup alone is not the major culprit in capacity loss. The

**ADVANCED
SCIENCE NEWS**
www.advancedsciencenews.com

**ADVANCED
MATERIALS
INTERFACES**
www.advmatinterfaces.de

most significant difference between the cycled cathodes lies in the content of SO_x and PO_x species. The presence of more oxygen-containing SE decomposition products for the PC-85 cathode suggests a higher degree of oxygen release during cycling, likely occurring in parallel to CAM cracking (O^{2-}/ S^{2-} exchange cannot be excluded though). It should be noted that the CAM is the only oxygen source at the cathode side and the oxygen, which is reactive in nature, can undergo follow-up reactions with the SE.[56] For the SC-83 cathode, particle fracture was virtually nonexistent, and the SE and CAM particles seemed to better maintain contact, ultimately resulting in improved capacity retention.

The atomic percentages of Ni, Co and Mn determined from XPS are shown in Figure S4 (Supporting Information). Both samples were found to be covered by the SE prior to cycling. After cycling, more intense signals were detected, especially for the PC-85 cathode, which agrees with the higher cracking susceptibility of the secondary particles (see Figures 3b,c).

Finally, STEM imaging, EELS mapping and in situ gas analysis were conducted to corroborate the XPS results. The STEM images in **Figure 5**a show that the PC-85 CAM was severely cracked, while no significant fracture or change in particle morphology was observed for the SC-83 sample after 200 cycles. According to EELS mapping, an oxygen-rich decomposition interphase formed in the cracked regions, which helps explain the differences in the content of oxygenated species.

The gassing behavior was probed using DEMS.[56,57] To this end, cells with an In anode were assembled and cycled at a rate of C/20 and 45 °C between 2.3 and 4.4 V versus In/InLi. Similar specific charge capacities were achieved for the different cells. The $m/z = 32$ signal, referring to O_2, was clearly visible near the end of the charge cycle, with an onset potential of ≈4.3 V versus Li^+/Li (Figure 5b). The O_2 evolution originates from the destabilization of the NCM lattice at states of charge beyond ≈80% and from the electrochemical carbonate oxidation.[47,57,58] The PC-85 cathode showed much more O_2 release. Because the carbonate content was very similar for the CAMs employed in the present work and the cells were identical otherwise, this finding can only be explained by the different cracking behavior (exposure of fresh and reactive surfaces) and interfacial contact between CAM and SE. More specifically, the lattice collapse (unfavorable H2-H3 transition in Ni-rich NCM cathodes) at high potentials is one of the main reasons leading to crack formation and growth and is further coupled with the occurrence of bulk oxygen redox.

2.5. Cycling Performance of the SC Cathode Material after Surface Coating

The above results demonstrate that the superior performance of the SC-83 CAM is directly related to its increased (micro) structural integrity and the continuous SE decomposition during electrochemical cycling is the main reason for the capacity fading of cells using the uncoated particles. Accordingly, the long-term cycling performance could be improved by forming stable interfaces. For this purpose, the surface of the SC-83 particles was coated with a nanoscale layer of $LiNbO_3$ (1.0 wt%, denoted as LNB), which is one of the most promising
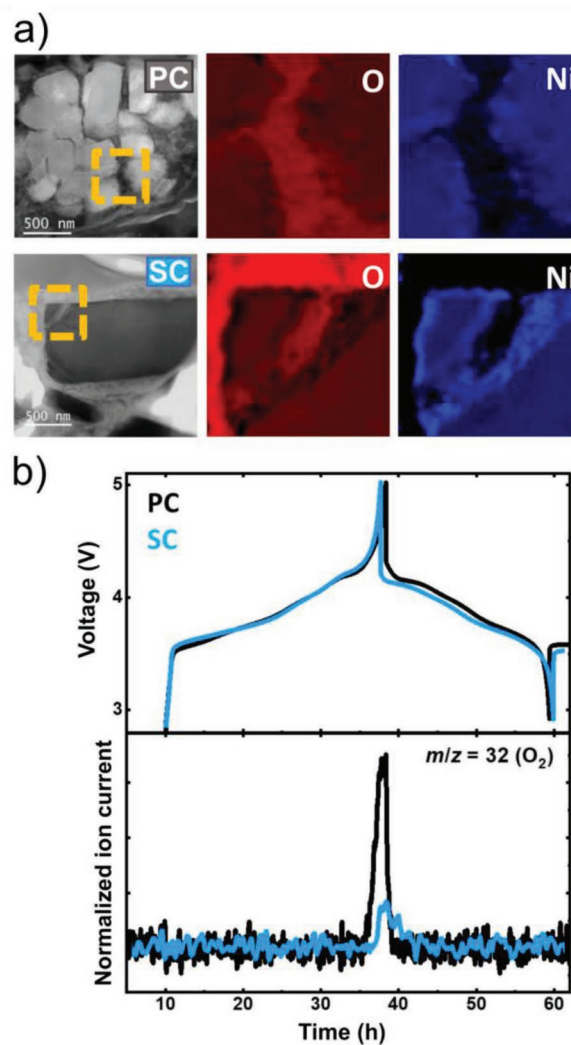

Figure 5. a) STEM imaging and EELS mapping of the PC-85 (black) and SC-83 (blue) CAM particles after cycling. b) In situ gas analysis. The initial voltage profiles of the ASSB cells cycled at C/20 rate and 45 °C between 2.3 and 4.4 V versus In/InLi (converted to voltage vs Li^+/Li) and corresponding normalized ion currents for O_2 are shown.

and widely used coating materials for NCM cathodes, aiming at isolating the SE from the CAM.[23,24,59] As can be seen from the data in **Figure 6**a, the initial CE increased to (82.2 ± 0.4)%. In addition, the cells delivered larger specific discharge capacities of (184 ± 2) mAh g_{NCM}^{-1} at C/10 (see voltage profiles at C/10 rate in Figure S5, Supporting Information), due to reduced interfacial resistance. This is confirmed by the Nyquist plots of the electrochemical impedance after 200 cycles shown in Figure S6 (Supporting Information), revealing the effectiveness of the coating in mitigating (electro)chemical side reactions. However, the rate capability in the initial cycles was similar for the cells using uncoated or $LiNbO_3$-coated SC-83 cathodes. Nevertheless, coating the SC-83 particles with a protective overlayer strongly increased the longevity, with capacity retentions of ≈93% after 200 cycles, compared to ≈79% for the uncoated CAM, and ≈80% after 400 cycles (Figure 6b and Figure S7, Supporting

**ADVANCED
SCIENCE NEWS**

www.advancedsciencenews.com

**ADVANCED
MATERIALS
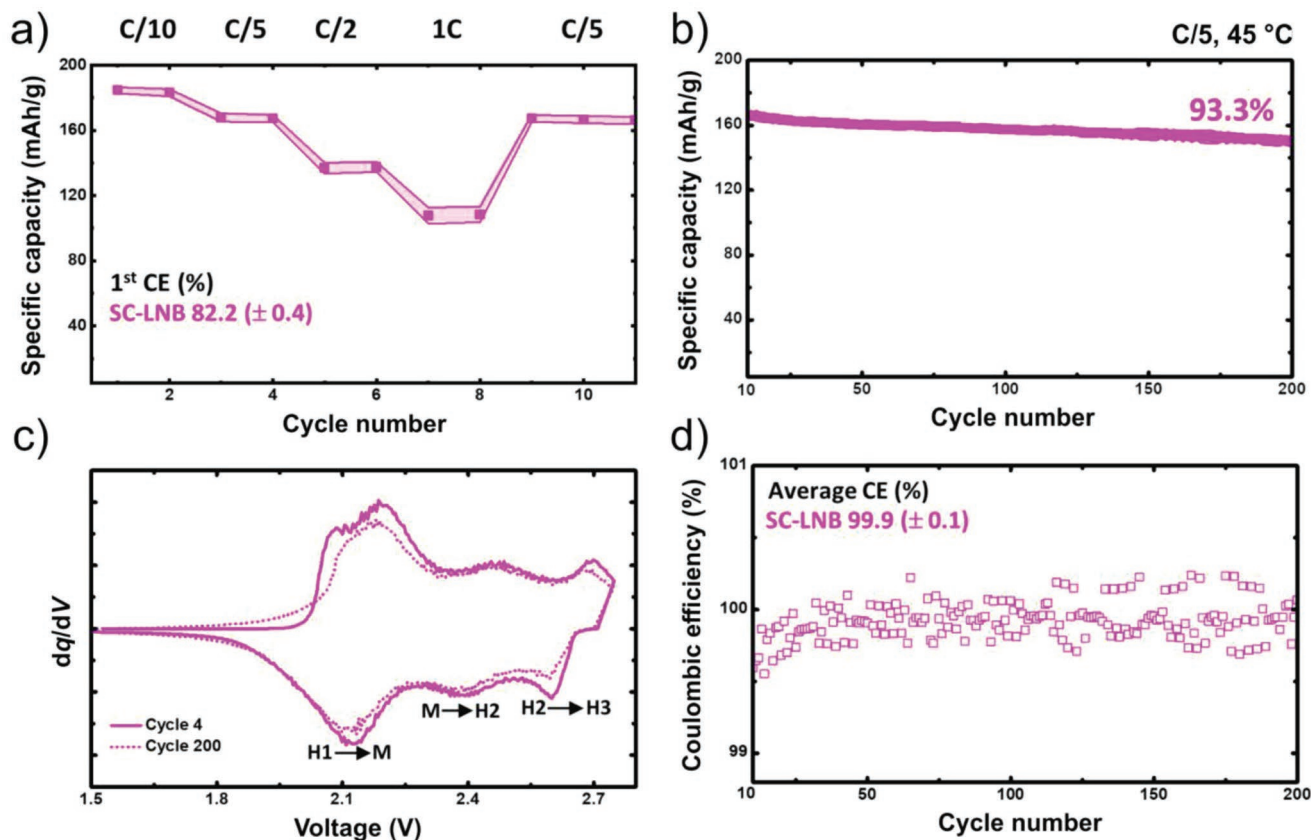INTERFACES**

www.advmatinterfaces.de

Figure 6. a) Rate performance of the ASSB cells with LiNbO$_3$-coated SC-83 cathode. b) Long-term cycling performance at C/5 after initial rate capability testing. c) Differential capacity plots for the 4th and 200th cycles. d) Coulomb efficiencies. The cells were cycled at 45 °C between 1.35 and 2.75 V versus Li$_4$Ti$_5$O$_{12}$/Li$_7$Ti$_5$O$_{12}$. The data are the average of three independent cells.

Information). This is among the best performances seen in the literature for high-loading (pelletized) cells with a Ni-rich NCM cathode and a sulfide-based SE.[33,40,45] The improvements in cyclability are also apparent from the differential capacity curves in Figure 6c and the CE in Figure 6d. The latter stabilized more quickly at (99.9 ± 0.1)%.

The excellent cycling performance is attributed to two effects. First, as described in the previous sections, the SC-83 CAM remains largely crack-free and further maintains tight contact with the SE particles. Second, the protective coating helps to stabilize the SE|CAM interface by suppressing SE decomposition. Overall, the combination of these two effects positively impacts the electro-chemo-mechanical behavior of the cathode in the ASSB cells.

3. Conclusion

In summary, this work compared the cyclability of bulk-type ASSB full cells with SC and PC Ni-rich NCM CAMs. Uncoated SC cathodes were found to exhibit superior performance over the PC counterparts, due to lower susceptibility for particle fracture and contact loss, among others. The improved crack resistance also had a positive impact on the gas evolution, especially the release of oxygen from the NCM lattice, thus somewhat altering the nature of the SE|CAM decomposition interphase. Nevertheless, both the uncoated SC and PC cathodes suffered from severe side reactions resulting from the (electro)chemical SE oxidation during cycling. Applying a LiNbO$_3$ coating to the SC CAM particles helped to mitigate the cathode interface degradation. The respective cells were capable of delivering specific discharge capacities of ≈160 mAh g$_{NCM}^{-1}$ at C/5 rate and 45 °C, with a capacity retention of 93.3% after 200 cycles. Overall, this study demonstrates that mechanically robust CAM particle morphologies are beneficial to the performance of ASSBs and proper coating enables stable cycling by addressing the adverse effects of side reactions.

4. Experimental Section

Electrode Preparation: Both PC-85 and SC-83 were received from BASF SE. The latter CAM was used as received, while the former was heated in O$_2$ flow at 750 °C for 3 h to reduce the amount of residual surface carbonates. The cathode composites were made by mixing (69:30:1 by weight) the NCM CAM, Li$_6$PS$_5$Cl SE (NEI Corp.), and Super C65 carbon black additive (Timcal). The anode composite was prepared by mixing carbon-coated Li$_4$Ti$_5$O$_{12}$ (NEI Corp.), Li$_6$PS$_5$Cl, and Super C65 with a weight ratio of 30:60:10. Both cathode and anode composites were milled for 30 min at 140 rpm under an Ar atmosphere using 10 zirconia balls in a planetary mill (Fritsch).

LiNbO$_3$ Coating: 410 µL of lithium ethoxide (1.0 M) and 820 µL of niobium ethoxide (0.5 M) in absolute ethanol were added to 6.0 g CAM in an Ar-filled glove box. The container was sealed, taken out from the glove box and treated in an ultrasonic bath for 30 min. The mixture

2201806 (7 of 9)

was then dried in a vacuum overnight until the solvent was completely removed. Finally, the powder was ground using a mortar and pestle in the glove box, followed by heating in O_2 at 350 °C (5 °C min^{-1} heating rate) for 2 h.[59]

Cell Assembly and Testing: The electrochemical performance was studied using a customized cell setup with two stainless steel dies and a PEEK sleeve (10 mm diameter). First, 100 mg SE was compressed at 63 MPa. In the next step, 12.0–12.5 mg cathode composite (2.0–2.1 mAh cm^{-2}) and 64–66 mg anode composite were placed on different sides of the SE pellet (n/p ratio of ≈2.1) and pressed at 375 MPa. Galvanostatic (dis)charge measurements were conducted at 45 °C in the voltage range 1.35–2.75 V versus $Li_4Ti_5O_{12}/Li_7Ti_5O_{12}$ (i.e., ≈2.9–4.3 V vs Li$^+$/Li) using a MACCOR battery cycler. All cells were assembled in an Ar-filled glove box. A theoretical specific capacity of 190 mAh g_{NCM}^{-1} (1C = 190 mA g_{NCM}^{-1}) was considered for the CAMs employed in this work. A pressure of 80 MPa was maintained during the electrochemical testing.

Surface Characterization: XPS data were acquired using a Thermo Scientific Kα spectrometer with an Al Kα X-ray source (1486.6 eV, 400 μm spot size). Spectra were recorded with a concentric hemispherical analyzer at a pass energy of 50 eV and fit with one or more Voigt profiles (±0.2 eV binding energy uncertainty). Scofield sensitivity factors were applied for quantification using the Avantage software package.[60] All spectra were referenced to the C1s peak (C—C, C—H) at a binding energy of 285.0 eV, controlled by means of the photoelectron peaks of Cu, Ag, and Au.

Electron Microscopy: A Zeiss Leo 1530 microscope equipped with a field emission source was used for SEM. TEM (incl. STEM, EDS and EELS) was conducted on specimens at 300 kV using a double-corrected Themis-Z microscope (Thermo Fisher Scientific). Specimen cross-sections were prepared by means of a dual-beam focused Ga-ion beam in an FEI Strata 400 at 30 kV, followed by cleaning at 5 and 2 kV.

In Situ Gas Analysis: For the DEMS cells, a similar assembly process to that described above was used, except that In metal served as anode. They were assembled in a PEEK ring and then placed in the DEMS setup. Cycling was performed at a rate of C/20 and 45 °C in the voltage range 2.3–4.4 V versus In/InLi (i.e., ≈2.9–5.0 V vs Li$^+$/Li) using a VSP-300 potentiostat (BioLogic). The cells underwent a 10 h OCV period for temperature and background stabilization. A mass flow controller (F-201CV; Bronkhorst) was used to tailor the He gas flow (2.5 mL min^{-1}, purity 6.0) and a mass spectrometer (OmniStar GSD 320 O; Pfeiffer Vacuum GmbH) for gas analysis.

In Situ Pressure Measurements: The rigid custom frame used to maintain the stack pressure during cycling was modified to accommodate an additional force sensor (ME-Meßsysteme KM26 10 kN). The sensor was attached to the sealed cell, and an initial pressure of 80 MPa was set. The setup was placed in a heating chamber at 45 °C. After 24 h OCV, the cells were cycled at C/10 rate and 45 °C between 1.35 and 2.75 V versus $Li_4Ti_5O_{12}/Li_7Ti_5O_{12}$ using a VMP3 multichannel potentiostat (BioLogic).

Acid Titration: To determine the carbonate content, acid titration coupled with mass spectrometry measurements were conducted on the CAMs. The setup consisted of a glass vial containing the sample, which was sealed with a septum and connected to a mass spectrometer (HiCube Pro with a PrismaPlus detector; Pfeiffer Vacuum GmbH) and a mass flow controller. Ar was used as carrier gas at a flow rate of 2.5 mL min^{-1}. 10 mg CAM was exposed to ≈0.35 mL H_2SO_4 (1 M), and a calibration gas for quantification was passed through the system after each run.

Statistics: Electrochemical data are the average of two or three independent battery cells. Both mean value and standard deviation were determined via "Statistics on Rows" using OriginPro 2020 (OriginLab Corp.).

Supporting Information

Supporting Information is available from the Wiley Online Library or from the author.

Conflict of Interest

The authors declare no conflict of interest.

Data Availability Statement

The data that support the findings of this study are available from the corresponding author upon reasonable request.

[1] J. C. Bachman, S. Muy, A. Grimaud, H.-H. Chang, N. Pour, S. F. Lux, O. Paschos, F. Maglia, S. Lupart, P. Lamp, L. Giordano, Y. Shao-Horn, *Chem. Rev.* **2016**, *116*, 140.

[2] Y. Kato, S. Hori, T. Saito, K. Suzuki, M. Hirayama, A. Mitsui, M. Yonemura, H. Iba, R. Kanno, *Nat. Energy* **2016**, *1*, 16030.

[3] R. Sahore, F. Dogan, I. D. Bloom, *Chem. Mater.* **2019**, *31*, 2884.

[4] L. Liu, J. Xu, S. Wang, F. Wu, H. Li, L. Chen, *eTransportation* **2019**, *1*, 100010.

[5] S. Randau, D. A. Weber, O. Kötz, R. Koerver, P. Braun, A. Weber, E. Ivers-Tiffée, T. Adermann, J. Kulisch, W. G. Zeier, F. H. Richter, J. Janek, *Nat. Energy* **2020**, *5*, 259.

[6] Y. Zhu, X. He, Y. Mo, *ACS Appl. Mater. Interfaces* **2015**, *7*, 23685.

[7] F. Zhang, Q.-A. Huang, Z. Tang, A. Li, Q. Shao, L. Zhang, X. Li, J. Zhang, *Nano Energy* **2020**, *70*, 104545.

[8] J. H. Teo, F. Strauss, F. Walther, Y. Ma, S. Payandeh, T. Scherer, M. Bianchini, J. Janek, T. Brezesinski, *Mater. Futures* **2022**, *1*, 015102.

[9] Z. Wu, Z. Xie, A. Yoshida, Z. Wang, X. Hao, A. Abudula, G. Guan, *Renewable Sustainable Energy Rev.* **2019**, *109*, 367.

[10] P. Yao, H. Yu, Z. Ding, Y. Liu, J. Lu, M. Lavorgna, J. Wu, X. Liu, *Front. Chem.* **2019**, *7*, 522.

[11] X. Yang, M. Jiang, X. Gao, D. Bao, Q. Sun, N. Holmes, H. Duan, S. Mukherjee, K. Adair, C. Zhao, J. Liang, W. Li, J. Li, Y. Liu, H. Huang, L. Zhang, S. Lu, Q. Lu, R. Li, C. V. Singh, X. Sun, *Energy Environ. Sci.* **2020**, *13*, 1318.

[12] H. Chen, Q.-y. Liu, M.-x. Jing, F. Chen, W.-y. Yuan, B.-w. Ju, F.-y. Tu, X.-q. Shen, S.-b. Qin, *ACS Appl. Mater. Interfaces* **2020**, *12*, 15120.

[13] Q. Liu, Z. Geng, C. Han, Y. Fu, S. Li, Y.-b. He, F. Kang, B. Li, *J. Power Sources* **2018**, *389*, 120.

[14] R. Grissa, S. Payandeh, M. Heinz, C. Battaglia, *ACS Appl. Mater. Interfaces* **2021**, *13*, 14700.

[15] W. S. Tang, K. Yoshida, A. V. Soloninin, R. V. Skoryunov, O. A. Babanova, A. V. Skripov, M. Dimitrievska, V. Stavila, S.-i. Orimo, T. J. Udovic, *ACS Energy Lett.* **2016**, *1*, 659.

**ADVANCED
Science News**

www.advancedsciencenews.com

**ADVANCED
MATERIALS
INTERFACES**

www.advmatinterfaces.de

[16] L. Duchêne, A. Remhof, H. Hagemann, C. Battaglia, *Energy Storage Mater.*. **2020**, *25*, 782.

[17] S. H. Payandeh, D. Rentsch, Z. Łodziana, R. Asakura, L. Bigler, R. Černý, C. Battaglia, A. Remhof, *Adv. Funct. Mater.* **2021**, *31*, 2010046.

[18] J. B. Grinderslev, M. B. Amdisen, L. N. Skov, K. T. Møller, L. G. Kristensen, M. Polanski, M. Heere, T. R. Jensen, *J. Alloys Compd.* **2022**, *896*, 163014.

[19] L. Zhou, T.-T. Zuo, C. Y. Kwok, S. Y. Kim, A. Assoud, Q. Zhang, J. Janek, L. F. Nazar, *Nat. Energy* **2022**, *7*, 83.

[20] L. M. Riegger, R. Schlem, J. Sann, W. G. Zeier, J. Janek, *Angew. Chem., Int. Ed.* **2021**, *60*, 6718.

[21] X. Li, J. Liang, X. Yang, K. R. Adair, C. Wang, F. Zhao, X. Sun, *Energy Environ. Sci.* **2020**, *13*, 1429.

[22] Q. Zhang, D. Cao, Y. Ma, A. Natan, P. Aurora, H. Zhu, *Adv. Mater.* **2019**, *31*, 1901131.

[23] S. P. Culver, R. Koerver, W. G. Zeier, J. Janek, *Adv. Energy Mater.* **2019**, *9*, 1900626.

[24] F. Walther, F. Strauss, X. Wu, B. Mogwitz, J. Hertle, J. Sann, M. Rohnke, T. Brezesinski, J. Janek, *Chem. Mater.* **2021**, *33*, 2110.

[25] A.-Y. Kim, F. Strauss, T. Bartsch, J. H. Teo, T. Hatsukade, A. Mazilkin, J. Janek, P. Hartmann, T. Brezesinski, *Chem. Mater.* **2019**, *31*, 9664.

[26] W. Jiang, X. Zhu, R. Huang, S. Zhao, X. Fan, M. Ling, C. Liang, L. Wang, *Adv. Energy Mater.* **2022**, *12*, 2103473.

[27] D. Lee, H. Lee, T. Song, U. Paik, *Adv. Energy Mater.* **2022**, *12*, 2200948.

[28] S. Sun, C.-Z. Zhao, H. Yuan, Y. Lu, J.-K. Hu, J.-Q. Huang, Q. Zhang, *Mater. Futures* **2022**, *1*, 012101.

[29] P. Minnmann, F. Strauss, A. Bielefeld, R. Ruess, P. Adelhelm, S. Burkhardt, S. L. Dreyer, E. Trevisanello, H. Ehrenberg, T. Brezesinski, F. H. Richter, J. Janek, *Adv. Energy Mater.* **2022**, *12*, 2201425.

[30] C. Wang, J. Liang, Y. Zhao, M. Zheng, X. Li, X. Sun, *Energy Environ. Sci.* **2021**, *14*, 2577.

[31] X. Liu, B. Zheng, J. Zhao, W. Zhao, Z. Liang, Y. Su, C. Xie, K. Zhou, Y. Xiang, J. Zhu, H. Wang, G. Zhong, Z. Gong, J. Huang, Y. Yang, *Adv. Energy Mater.* **2021**, *11*, 2003583.

[32] C. Doerrer, I. Capone, S. Narayanan, J. Liu, C. R. M. Grovenor, M. Pasta, P. S. Grant, *ACS Appl. Mater. Interfaces* **2021**, *13*, 37809.

[33] S. Payandeh, D. Goonetilleke, M. Bianchini, J. Janek, T. Brezesinski, *Curr. Opin. Electrochem.* **2022**, *31*, 100877.

[34] K. Ishidzu, Y. Oka, T. Nakamura, *Solid State Ionics* **2016**, *288*, 176.

[35] H.-H. Ryu, K.-J. Park, C. S. Yoon, Y.-K. Sun, *Chem. Mater.* **2018**, *30*, 1155.

[36] L. de Biasi, A. O. Kondrakov, H. Geßwein, T. Brezesinski, P. Hartmann, J. Janek, *J. Phys. Chem. C* **2017**, *121*, 26163.

[37] F. Strauss, L. de Biasi, A.-Y. Kim, J. Hertle, S. Schweidler, J. Janek, P. Hartmann, T. Brezesinski, *ACS Mater. Lett.* **2020**, *2*, 84.

[38] G. Qian, Y. Zhang, L. Li, R. Zhang, J. Xu, Z. Cheng, S. Xie, H. Wang, Q. Rao, Y. He, Y. Shen, L. Chen, M. Tang, Z.-F. Ma, *Energy Storage Mater.*. **2020**, *27*, 140.

[39] X. Li, W. Peng, R. Tian, D. Song, Z. Wang, H. Zhang, L. Zhu, L. Zhang, *Electrochim. Acta* **2020**, *363*, 137185.

[40] Y. Han, S. H. Jung, H. Kwak, S. Jun, H. H. Kwak, J. H. Lee, S.-T. Hong, Y. S. Jung, *Adv. Energy Mater.* **2021**, *11*, 2100126.

[41] R. Fantin, E. Trevisanello, R. Ruess, A. Pokle, G. Conforto, F. H. Richter, K. Volz, J. Janek, *Chem. Mater.* **2021**, *33*, 2624.

[42] A. N. Mansour, C. A. Melendres, *Surf. Sci. Spectra* **1994**, *3*, 271.

[43] D. Pritzl, T. Teufl, A. T. S. Freiberg, B. Strehle, J. Sicklinger, H. Sommer, P. Hartmann, H. A. Gasteiger, *J. Electrochem. Soc.* **2019**, *166*, A4056.

[44] Y. Ma, J. H. Teo, F. Walther, Y. Ma, R. Zhang, A. Mazilkin, Y. Tang, D. Goonetilleke, J. Janek, M. Bianchini, T. Brezesinski, *Adv. Funct. Mater.* **2022**, *32*, 2111829.

[45] C. Wang, R. Yu, S. Hwang, J. Liang, X. Li, C. Zhao, Y. Sun, J. Wang, N. Holmes, R. Li, H. Huang, S. Zhao, L. Zhang, S. Lu, D. Su, X. Sun, *Energy Storage Mater.*. **2020**, *30*, 98.

[46] T. Shi, Y.-Q. Zhang, Q. Tu, Y. Wang, M. C. Scott, G. Ceder, *J. Mater. Chem. A* **2020**, *8*, 17399.

[47] R. Jung, M. Metzger, F. Maglia, C. Stinner, H. A. Gasteiger, *J. Electrochem. Soc.* **2017**, *164*, A1361.

[48] E. Trevisanello, R. Ruess, G. Conforto, F. H. Richter, J. Janek, *Adv. Energy Mater.* **2021**, *11*, 2003400.

[49] S. Wang, W. Zhang, X. Chen, D. Das, R. Ruess, A. Gautam, F. Walther, S. Ohno, R. Koerver, Q. Zhang, W. G. Zeier, F. H. Richter, C.-W. Nan, J. Janek, *Adv. Energy Mater.* **2021**, *11*, 2100654.

[50] R. Koerver, W. Zhang, L. de Biasi, S. Schweidler, A. O. Kondrakov, S. Kolling, T. Brezesinski, P. Hartmann, W. G. Zeier, J. Janek, *Energy Environ. Sci.* **2018**, *11*, 2142.

[51] W. Zhang, D. Schröder, T. Arlt, I. Manke, R. Koerver, R. Pinedo, D. A. Weber, J. Sann, W. G. Zeier, J. Janek, *J. Mater. Chem. A* **2017**, *5*, 9929.

[52] M. M. Thackeray, K. Amine, *Nat. Energy* **2021**, *6*, 683.

[53] J. Auvergniot, A. Cassel, D. Foix, V. Viallet, V. Seznec, R. Dedryvère, *Solid State Ionics* **2017**, *300*, 78.

[54] S. Wang, M. Tang, Q. Zhang, B. Li, S. Ohno, F. Walther, R. Pan, X. Xu, C. Xin, W. Zhang, L. Li, Y. Shen, F. H. Richter, J. Janek, C.-W. Nan, *Adv. Energy Mater.* **2021**, *11*, 2101370.

[55] C. Yu, L. van Eijck, S. Ganapathy, M. Wagemaker, *Electrochim. Acta* **2016**, *215*, 93.

[56] T. Bartsch, F. Strauss, T. Hatsukade, A. Schiele, A.-Y. Kim, P. Hartmann, J. Janek, T. Brezesinski, *ACS Energy Lett.* **2018**, *3*, 2539.

[57] F. Strauss, J. H. Teo, A. Schiele, T. Bartsch, T. Hatsukade, P. Hartmann, J. Janek, T. Brezesinski, *ACS Appl. Mater. Interfaces* **2020**, *12*, 20462.

[58] F. Strauss, S. Payandeh, A. Kondrakov, T. Brezesinski, *Mater. Futures* **2022**, *1*, 023501.

[59] S. Payandeh, F. Strauss, A. Mazilkin, A. Kondrakov, T. Brezesinski, *Nano Res. Energy* **2022**, https://doi.org/10.26599/NRE.2022.9120016.

[60] J. H. Scofield, *J Electron Spectrosc. Relat. Phenom.* **1976**, *8*, 129.